

# Multi-Component PtFeCoNi Core-Shell Nanoparticles on MWCNTs as Promising Bifunctional Catalyst for Oxygen Reduction and Oxygen Evolution Reactions

Tobias Braun,<sup>\*,[a]</sup> Sirshendu Dinda,<sup>[a]</sup> Guruprakash Karkera,<sup>[a]</sup> Georgian Melinte,<sup>[a, b]</sup> Thomas Diemant,<sup>[a]</sup> Christian Kübel,<sup>[b, c, d]</sup> Maximilian Fichtner,<sup>[a, b]</sup> and Frank Pammer<sup>\*,[a]</sup>

The development of commercially viable fuel cells and metal-air batteries requires effective and cheap bifunctional catalysts for the oxygen reduction reaction (ORR) and the oxygen evolution reaction (OER). Multi-component Pt–Fe–Co–Ni nanoparticles on multi-walled carbon nanotubes (MWCNTs) were synthesized by wet chemistry route via NaBH<sub>4</sub> reduction of metal salts, followed by sintering at different temperatures. The catalyst demonstrates an excellent ORR activity and a promising OER activity in 0.1 M KOH, with a bi-functional over-

potential,  $\Delta E$  of 0.83 V, which is comparable to the values of Pt/C or RuO<sub>2</sub>. Furthermore, it shows outstanding long-term stability in ORR and OER, namely diffusion limited current density at a potential of 0.3 V decreased just by 5.5% after 10000 cycles in ORR. The results of the PFCN@NT<sup>300</sup> indicate a significant effect of the substitution of Pt by the transition metal (TM) and the formation of nanoparticles on the catalytic performance, especially in the OER.

## Introduction

Fuel cells (FCs)<sup>[1–3]</sup> and metal-air batteries (MABs)<sup>[4–6]</sup> are expected to play an important role in the successful transition from a fossil fuel based economy to a an economy powered by clean, renewable and sustainable energy sources. The oxygen electrode reactions in both types of devices are the oxygen reduction reaction (ORR) and the oxygen evolution reaction (OER). Typically, the reaction mechanisms of the ORR and OER differs depending on the type of electrolyte used (acidic or

alkaline media). The ORR either proceeds via a one-step-four-electron or a two-step-two-electron transfer mechanism, while for the OER a four-electron transfer is common.<sup>[7,8]</sup> In both reactions oxygen-containing intermediates such as \*O, \*OH and \*OOH are involved. The rate limiting steps for ORR were shown to be the reduction of \*OH and O<sub>2</sub>,<sup>[9]</sup> while for OER the slowest steps are the formation of \*OOH and \*O.<sup>[9,10]</sup> The sluggish kinetics of both reactions require the use of a stable bifunctional catalyst. Highly effective state-of-the-art catalysts for ORR are Pt-based materials such as PtCo alloy nanoparticles,<sup>[11–14]</sup> whereas IrO<sub>2</sub> and RuO<sub>2</sub> are efficient OER catalysts.<sup>[15,16]</sup> A quick and easy accessible way to achieve bifunctional catalytic performance is by composites, where a ORR and a OER active material will be mixed together, such as Pt and IrO<sub>2</sub><sup>[17,18]</sup> or Pt and RuO<sub>2</sub>.<sup>[19]</sup> However, the development of economically viable, effective and stable bifunctional catalysts made from low cost transition metals (TMs) remains an open challenge for future reversible oxygen applications.<sup>[20]</sup>

Some key parameters have been defined to compare the catalytic activity between various materials. The slope of the ORR polarization curve contains the half-wave potential  $E_{1/2}$  and the corresponding current density  $j_{1/2}$ , which defines the geometrical activity of the catalysts. The slope of the OER polarization curve defines the over-potential  $E_{10}$  at the point where the current density  $j_{10}$  reaches 10 mA cm<sup>-2</sup>. Finally, the total over-potential  $\Delta E$  describes potential difference between  $j_{1/2}$  and  $j_{10}$ . The value of  $\Delta E$  allows a quick comparison and evaluation of different catalysts.<sup>[7]</sup> Pure Pt-catalysts have a  $\Delta E$ -value of 1.04 V and Pt/IrO<sub>2</sub> with a ratio of 1:9 shows a  $\Delta E$  of 0.71 V.<sup>[17]</sup>

A preferred, but more difficult method is the use of one material for both reactions. Thereby, it is possible to increase the stability and reduce materials costs. The noble metal can be partially replaced for example by transition metals (oxides) to achieve high activity with a low  $\Delta E$ . There are a few studies


[a] Dr. T. Braun, Dr. S. Dinda, Dr. G. Karkera, Dr. G. Melinte, Dr. T. Diemant, Prof. Dr. M. Fichtner, Dr. F. Pammer  
Helmholtz Institute Ulm,  
Helmholtzstraße 11,  
89081 Ulm, Germany


E-mail: frank.pammer@kit.edu  
1.tobias.braun@gmail.com

[b] Dr. G. Melinte, Prof. Dr. C. Kübel, Prof. Dr. M. Fichtner  
Institute of Nanotechnology,  
Karlsruhe Institute of Technology (KIT),  
Hermann-von-Helmholtz-Platz 1,  
76344 Eggenstein-Leopoldshafen, Germany

[c] Prof. Dr. C. Kübel  
Department of Materials and Earth Sciences,  
Technical University of Darmstadt,  
Alarich-Weiss-Straße 2, 64287 Darmstadt, Germany

[d] Prof. Dr. C. Kübel  
Karlsruhe Nano Micro Facility (KNMF),  
Karlsruhe Institute of Technology,  
Hermann-von-Helmholtz-Platz 1,  
76344 Eggenstein-Leopoldshafen, Germany

 Supporting information for this article is available on the WWW under <https://doi.org/10.1002/slct.202300396>

 © 2023 The Authors. ChemistrySelect published by Wiley-VCH GmbH. This is an open access article under the terms of the Creative Commons Attribution Non-Commercial License, which permits use, distribution and reproduction in any medium, provided the original work is properly cited and is not used for commercial purposes.

about multi-component Pt-TM catalysts and their electrochemical ORR activity,<sup>[19,21,22]</sup> however there is no report about quaternary PtFeCoNi nanoparticles with a TM-oxide shell and a Pt-core that show both excellent activity and long-term stability in ORR, while also providing promising performance in OER.

Herein, we report the synthesis of multi-component Pt–Fe–Co–Ni nanoparticles on multi-walled carbon nanotubes (MWCNTs) via reduction with NaBH<sub>4</sub>. Their catalytic activity in ORR was investigated in alkaline media by rotating (ring) disk electrode measurements before and after sintering, while the long-term stability and the OER activity was determined only for the sintered catalyst. The prepared catalysts were characterized by a number of techniques in order to reveal their structural and chemical properties, including X-ray diffraction (XRD), X-ray fluorescence analysis (XRF), X-ray photoelectron spectroscopy (XPS), high-angle annular dark-field scanning transmission electron microscopy (HAADF STEM) and scanning electron microscopy (SEM) in combination with energy dispersive X-ray spectroscopy (EDX).

## Results and Discussion

Acid-functionalized MWCNT (*f*-MWCNT) were loaded with Pt–Fe–Co–Ni-containing nanoparticles (PFCN) via reduction of metal salts with NaBH<sub>4</sub>. Parts of the resulting composite PFCN@NT were further modified by sintering at either 300 °C under argon (PFCN@NT<sup>300</sup>) or at 600 °C under Ar/H<sub>2</sub> 95/5 atmosphere (PFCN@NT<sup>600</sup>). As shown in Figure 1a, the as-prepared sample PFCN@NT (—) exhibited severely broadened

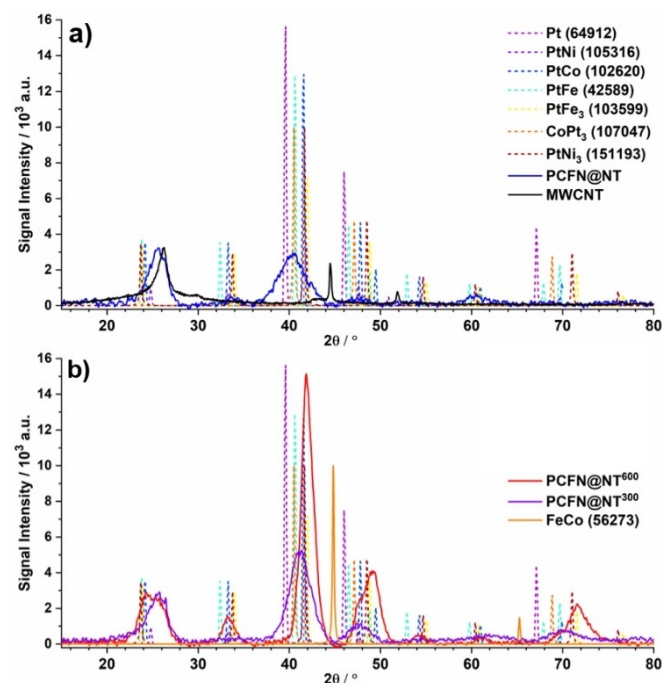


**Figure 1.** X-ray diffractograms of (a) MWCNT and PFCN@NT, and annealed samples (b) PFCN@NT<sup>300</sup> and PFCN@NT<sup>600</sup> superimposed with patterns of reference compounds from literature. ICSD registry numbers given in brackets.

peaks at  $\approx 26^\circ$ ,  $42^\circ$ , and  $61^\circ$ , that correspond to overlaying signals of MWCNT (—) and Pt (—) which confirms its composite formation with the graphitic structure. The XRD peak positions were slightly shifted to higher angles, relative to the standard Pt pattern (ICSD # 64912), i.e., the reflection at  $39.8^\circ$  was shifted to  $40.2^\circ$ , indicating that Fe, Co, Ni with smaller atomic radii, are incorporated into the Pt lattice to form other intermetallic alloy phases (e.g. PtNi<sub>3</sub> (—), PtFe (—), PtCo (—)) with smaller lattice parameters. After heat treatment at 300 °C and 600 °C (Figure 1b), crystallinity increases and more pronounced peaks appear at 24.3, 33.37, 54.25, 60.97 and  $71.6^\circ$ . The good agreement with the reference samples points to the consolidation of the PtNi<sub>3</sub> phase (—) and the absence of pure metallic Pt, as indicated by the lack of the Pt-signal at  $39.5^\circ$ . Further analyses, (see Figure 4) showed at partial separation of the PtNi-phase from Fe and Co. However, significant mismatch with XRD patterns of an FeCo-alloy (—, Figure 1b) and Co<sub>x</sub>Fe<sub>y</sub>O<sub>z</sub> oxides (not shown, ICSD #: 166200, 266257) indicates that these phases are absent.

Since preliminary electrochemical experiments (Figure S1) indicated a rather poor performance of the high-temperature sintered sample PFCN@NT<sup>600</sup>, further structural and chemical characterization was focussed on the samples PFCN@NT and PFCN@NT<sup>300</sup>, the results of this analysis are discussed in the following.

X-ray photoelectron spectroscopy (XPS) was used to determine the elemental composition and analyze the oxidation state of the detected elements in the surface layer of the catalysts. First of all, the survey measurements (Figure S2) revealed the presence of Pt, Fe, Co, Ni, C and O, in both samples. As expected, the detail spectra of the C 1s region (Figure 2a) were dominated by the peak of the graphitic C atoms in the MWCNTs (sp<sup>2</sup>-C) at 284.6 eV, which was fitted using an asymmetric peak shape, i.e., with some tailing towards higher binding energy. In addition, the well-known  $\pi$ - $\pi^*$  satellite feature of graphitic C (at 291.0 eV) was also observed. Furthermore, peaks with much smaller intensity at 285.2, 286.5, and 288.6 eV could be assigned to C–H, C–O, and C=O species, respectively. Apart from the small Ni 3p feature at  $\sim 68.5$  eV, the Pt 4f detail spectra (Figure 2b) showed for both samples a single peak doublet at 71.6/74.9 eV, which is most probably related to metallic Pt species, since oxidized Pt species should appear at a binding energy well above 72 eV (e.g., the Pt 4f<sub>7/2</sub> peak of PtO is expected at  $\sim 74$  eV).<sup>[23,24]</sup> Compared to bulk metallic Pt,<sup>[23,24]</sup> the doublet is shifted by approximately 0.5 eV to higher binding energy, which indicates a positive partial charge on the Pt species. In contrast, the detail spectra of the first-row transition metals (Fe, Co and Ni, Figure 2c–e) clearly show the presence of oxidized metal species, while the presence of metallic states can be excluded for all three elements. Since XRD indicated the presence of metallic Ni and possible Fe and Co as well, we attribute the detection of oxides to surface oxidation of the nanoparticles. Ambient oxidation is expected to lead to formation of a ca. 1.5 nm thick oxide layer.<sup>[25]</sup> Given the limited penetration depth of XPS, which may account for the near exclusive detection of oxidized species. The observed positions of the 2p<sub>3/2</sub> peaks for all the three

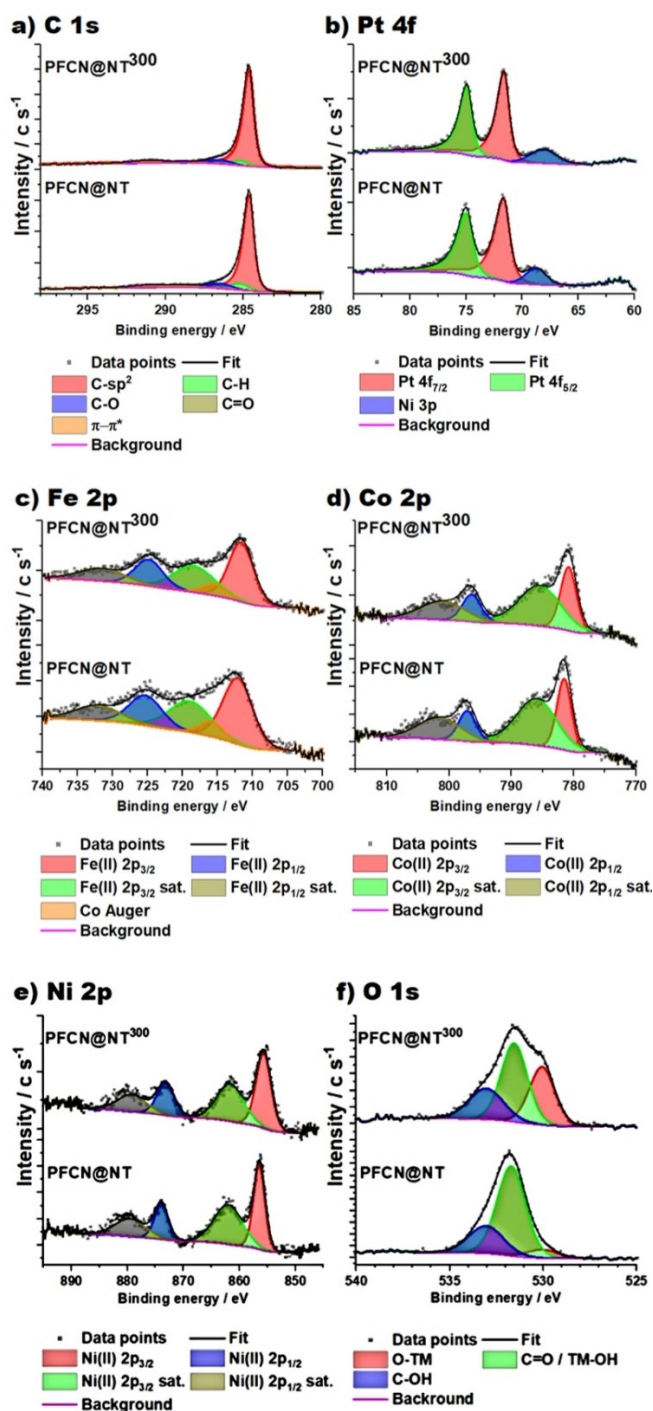


Figure 2. XPS detail spectra for the PFCN@NT and PFCN@NT<sup>300</sup> catalysts. Top: spectra, Bottom: Color-legend. sat. = satellite peak.

elements are typical for an oxidation state of +II or +III,<sup>[23,24]</sup> a distinction between these two possibilities is not possible based on the binding energy alone. This question is addressed again in more detail in the following paragraph when discussing the O1s spectra. Furthermore, significant satellite peaks are observed in all three regions (in addition a Co Auger feature interferes in the Fe 2p spectrum). Most interestingly a

shift by 0.5–0.8 eV to lower binding energy is observed for all three elements between sample PFCN@NT and PFCN@NT<sup>300</sup>. This negative shift could indicate a slight reduction of the average oxidation state and/or a change of the binding partners around the metal centers, we also come back to this in the next paragraph. Finally, we would like to discuss the detail spectra in the O 1s region (Figure 2f). The spectra could be fitted by three peaks. The first feature (at 530.0 eV) comes from the oxide anions of the first-row transition metals, the second one (at 531.6 eV) can be assigned both to metal hydroxide anions and C=O species, and the last peak (at 533.0 eV) is mainly caused by C–O functionalities. A significant reduction of the second peak (i.e., metal hydroxides) and growth of the first peak (i.e., metal oxides) is observed, when comparing the spectra of PFCN@NT to PFCN@NT<sup>300</sup>, which is most probably related to the annealing step to which PFCN@NT<sup>300</sup> was subjected. It is interesting to note that for the three first-row transition metals (Fe, Co and Ni), the 2p peaks of hydroxides tend to appear in general at higher binding energy than those of oxides of the same oxidation state<sup>[23,24]</sup> (e.g., 780.1 eV for CoO and 781.0 eV for Co(OH)<sub>2</sub><sup>[26]</sup>). Therefore, at least a part of the observed shift of the 2p peaks of the three metals when going from PFCN@NT to PFCN@NT<sup>300</sup> is most probably related to the partial change from hydroxide to oxide species between these two samples.

The results in the O 1s region can also be used for a rough estimation of the average oxidation state of the three metals (Fe, Co and Ni). For this purpose, we use the corrected intensities (considering the relative sensitivity factor) of the two features related to oxide and hydroxide species in the O 1s spectrum and compare to the sum of the intensities of the three metals. The contribution of C=O species to the hydroxide O 1s peak was removed by considering the intensity of the C=O peak in the C 1s spectra and assuming a C:O ratio of 1:1. Here, we make use of the fact that only C, O, Pt, Fe, Co and Ni were detected in the survey spectrum (H cannot be seen by XPS but is most probably also there), while the peaks of other elements like Cl or S from chlorides or (e.g.) sulfates were absent. This means that the most probable anions are oxides and hydroxides (or a mixture of it). The presence of metal carbonates is also possible; they contribute to the C=O peak in the C 1s spectra and to the C=O/hydroxide peak in the O 1s spectra. Our calculations showed 0.20 oxide and 1.32 hydroxide anions per metal atom M (M = Fe + Ni + Co) for PFCN@NT, while it was 0.60 oxide and 0.62 hydroxide anions per M in PFCN@NT<sup>300</sup>. Taking into account of the stoichiometry of oxides and hydroxides this translates to a calculated average oxidation state 1.72 for PFCN@NT and 1.82 for PFCN@NT<sup>300</sup> per M atom. Here, it is important to mention again the rather rough character of the estimation; consequently, the error margin can be expected to be rather large. In any case, this estimation indicates that for both samples the average oxidation state of the three metals Fe, Co, and Ni is rather in the range of +II than +III. Finally, it should be mentioned that in case of Co our assessment of a predominant oxidation state +II is also corroborated by the occurrence of the satellite features, since they are usually only observed for Co<sup>2+</sup>.<sup>[27]</sup>



Figure 3a shows the initial morphology of the PtFeCoNi nanoparticles and aggregates on the network of MWCNTs. Parts of the PtFeCoNi-nanoparticles appear aggregated into large agglomerations. Still, a significant number of individual nanoparticles that are up to 20 nm in size are dispersed on the MWCNTs surfaces. The particles generally exhibit an internal multi-core structure (Figure 4) with irregularly shaped metallic Pt cores of 2–5 nm in diameter that are embedded in a transition metal oxide matrix. The 300 °C heat treatment (PFCN@NT<sup>300</sup>, Figure 3b) does not result in discernable changes in the particle size or morphology. The same is true for the elemental distribution within isolated PFCN@NT<sup>300</sup> and PFCN@NT nanoparticles, as shown in Figure 4 and Figure S3 (see electronic supporting information).

Additionally the metal ratio of the catalyst was determined by X-ray fluorescence analysis (XRF) and energy dispersive X-ray spectroscopy (EDX), the results are shown in Figures S4 and S5. The average molar ratio of Pt:Fe:Co:Ni as determined by XRF is 1.4/1.1/1/1.1 while EDX yields a ratio of 1.2/1/1/1. The SEM images shows some small areas with accumulations of the metal particles, as shown before in the TEM images.

The catalyst loading on the MWCNT was determined by thermogravimetric analysis (TGA; N<sub>2</sub>/O<sub>2</sub> flow) as shown in Figure S3. The remaining weight minus the residual mass of f-MWCNT of the PFCN@NT is 40.5% which is very close to the desired loading of 40%. The sintered sample at 300 °C shows a remaining weight of 44% which is higher due to further oxidation of the catalyst surface during the sintering process.

Fe, Co and O appear fairly uniformly distributed throughout the particles. This confirms that the phase surrounding the Pt particles is indeed a TM-oxide shell. In the pristine samples (PFCN@NT) Ni is also homogeneously dispersed throughout the particles (Figure S3). However, it appears much less evenly distributed after sintering (PFCN@NT<sup>300</sup>, Figure 4). Instead, Ni rather accumulates around the Pt cores, which might indicate alloy formation. Pt/Ni alloys are known electro-catalysts,<sup>[28–31]</sup> which would explain the superior performance of PFCN@NT<sup>300</sup> (see below). However, the XPS analysis did not show the presence of Ni<sup>0</sup>, which rules out the formation of bulk Ni<sub>x</sub>Pt<sub>y</sub>-

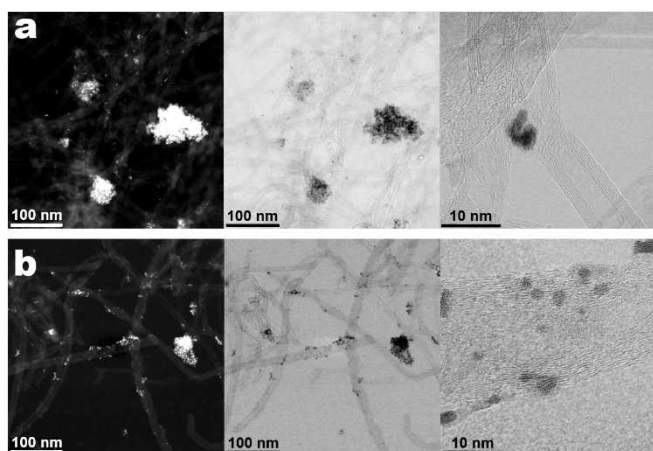


Figure 3. TEM images of a) PFCN@NT and b) PFCN@NT<sup>300</sup>.

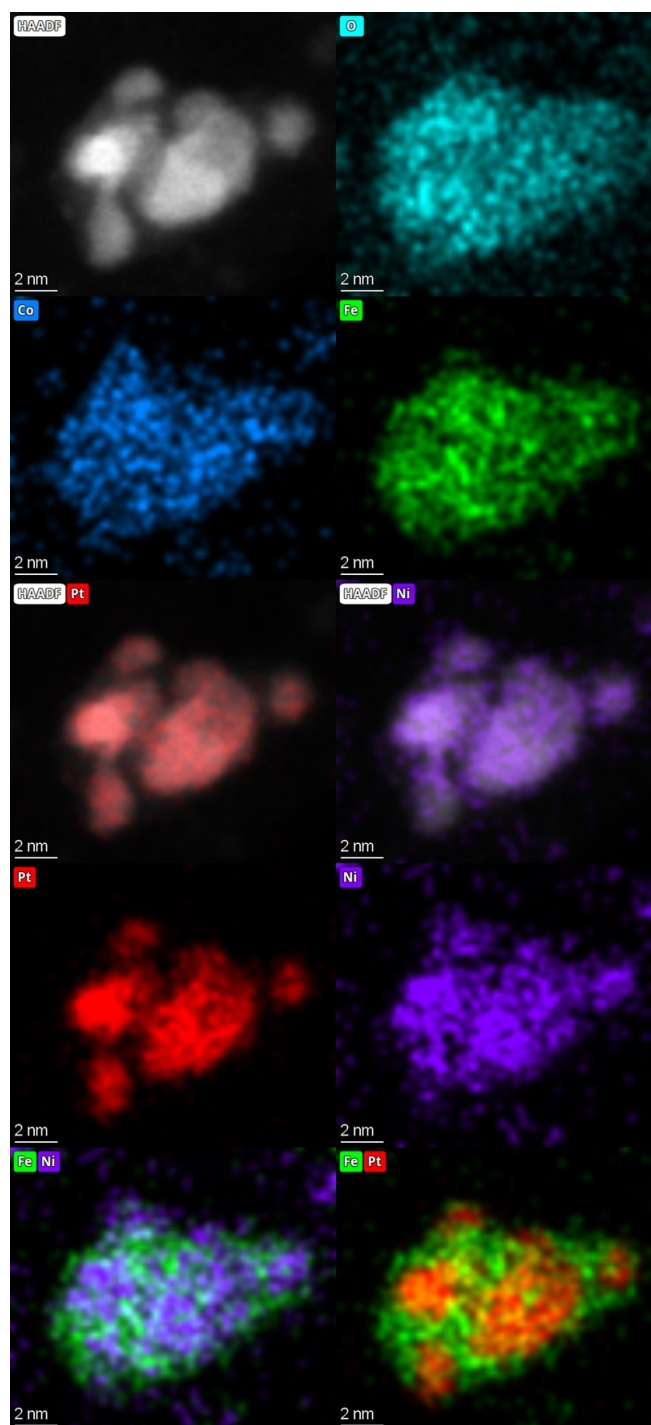
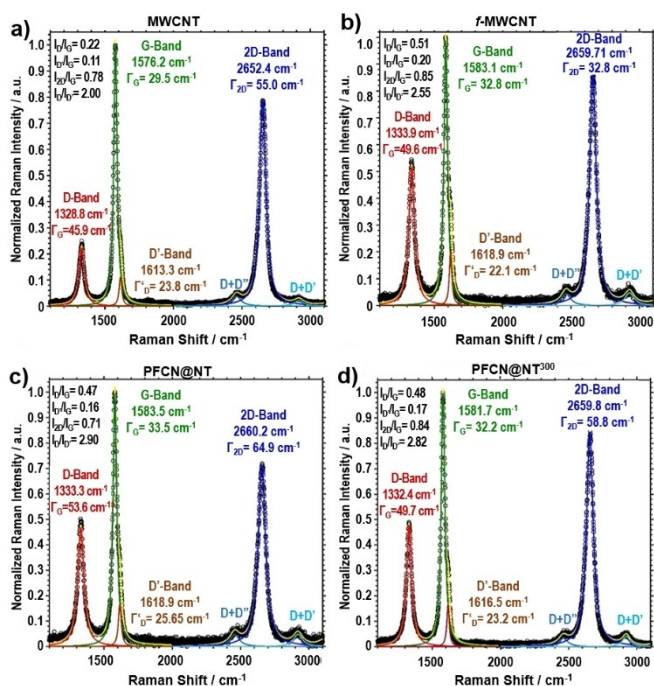


Figure 4. HAADF-Images and elemental distribution of an isolated PFCN@NT<sup>300</sup> nanoparticle.

nanoparticles.<sup>[28–31]</sup> Surface sites with elevated catalytic activity might still be present at the Pt/Ni-interface.

To elucidate the structural defect accumulation in the MWCNT backbone upon functionalization with the nanoparticles, we have performed the Raman spectral analysis of the pristine MWCNT and the materials from each step of the nano-composite preparation process. Figure 5a represents the



**Figure 5.** Normalized Raman spectra of the MWCNT and its nano-composite in successive preparation steps are presented. (a) MWCNT starting-material, (b) after acid-functionalisation (f-MWCNT) (c) loaded with nanoparticles (PFCN@NT), and (d) sintered at 300 °C (PFCN@NT<sup>300</sup>). All the spectra are recorded using a 633 nm excitation laser and 1 mW average power. Lorentzian lineshape function has been used to deconvolute all the Raman spectra.

Raman spectrum of pristine MWCNT and the deconvoluted components of the total Raman spectra. The D-band (~1328 cm<sup>-1</sup>), G-band (~1576 cm<sup>-1</sup>) and 2D-band (~2652 cm<sup>-1</sup>) are the most prominent and wellknown features of the MWCNT's honeycomb structure. (Merlen et al. 2017) The deconvolution of the Raman spectra also shows the D'-band (~1613 cm<sup>-1</sup>), a D + D'-band (~2462 cm<sup>-1</sup>) and a D + D'-band (~2920 cm<sup>-1</sup>), which indicates that the MWCNT is inherently disordered.<sup>[7]</sup> The value  $I_D/I_G$  gives the idea of the ordering of the honeycomb structure and hence the qualitative structural property of MWCNT in the process of nano-composite preparation. The  $I_D/I_G$  value increases from 0.22 to 0.51 when the MWCNT undergoes oxidation and remains almost unchanged in the following nano-composite synthesis processes. This suggests that, though the MWCNT becomes more disordered in the oxidation process, the value of  $I_D/I_G$  is much lower than 3.<sup>[32]</sup> The reduction and sintering processes have little to no effect on the MWCNT backbone which ensures that the nano-composite retains its ordered honeycomb structure. This ensures that the enhanced electrical conductivity of MWCNT is preserved throughout this elaborate nano-composite synthesis process. The overall structural integrity of MWCNT also remains almost intact after the synthesis.

Rotating ring-disk electrode (RRDE) measurements were performed to evaluate the electrochemical activities of the synthesized catalysts (Figure 6). ORR curves of PFCN@NT,

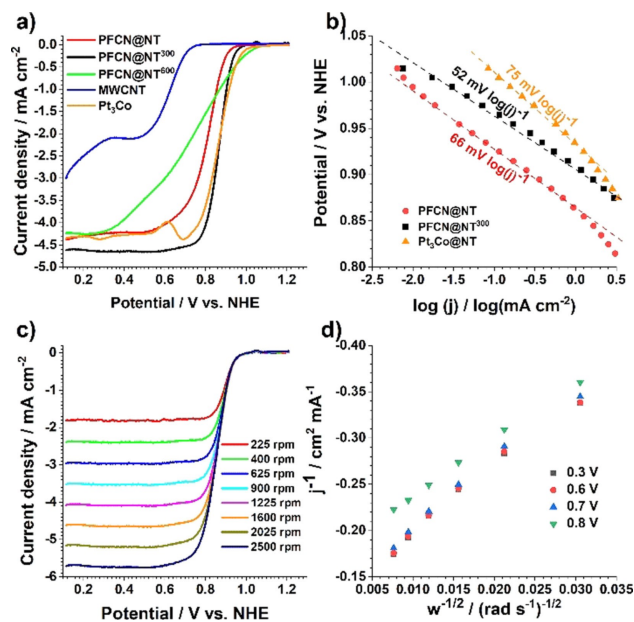


**Figure 6.** a) ORR curves of PFCN@NT, PFCN@NT<sup>300</sup>, PFCN@NT<sup>600</sup>, MWCNT and Pt<sub>3</sub>Co@NT at a rotation rate of 1600 rpm in 0.1 M KOH with a scan rate of 10 mV s<sup>-1</sup>. b) Tafel plots of PFCN@NT, PFCN@NT<sup>300</sup> and Pt<sub>3</sub>Co@NT. c) ORR curves of PFCN@NT<sup>300</sup> with different rotation rates. d) K–L plots of PFCN@NT<sup>300</sup> obtained from the RRDE results.

PFCN@NT<sup>300</sup>, PFCN@NT<sup>600</sup>, MWCNT and Pt<sub>3</sub>Co@NT were recorded in 0.1 M KOH at a rotation rate of 1600 rpm with a scan rate of 10 mV s<sup>-1</sup>. The synthesized catalysts showed enhanced electrochemical activity in ORR with more positive onset potentials and higher limiting current densities, compared to the MWCNT without metal-nanoparticles (Figure 6a). Overall the PFCN@NT<sup>300</sup> catalyst showed a slightly lower onset potential (953 mV) than the Pt rich Pt<sub>3</sub>Co@NT catalyst (983 mV, Table 1, entry 5, data analyzed according to equations (1), (2), and (3) in the experimental section). However, other performance parameters of this catalyst are equal or even better (see Table 1, entry 2). The slope of the Tafel-plot (see Figure 6b) shows for PFCN@NT<sup>300</sup> the lowest value of 52 mV log(j)<sup>-1</sup> of the tested catalysts. Figure 6c shows the ORR curves of PFCN@NT<sup>300</sup> at various rotation rates. The limiting current densities show constant distances between the different rotation rates (from 225 to 2500 rpm), in agreement with the theory of RRDE.<sup>[33–35]</sup> According to the Levich equation (see equations (1) and (2)), the limiting current densities are proportional to the square

**Table 1.** Electrocatalytic data for PFCN@NT-materials and reference catalysts.

Entry	Catalyst	E <sub>1/2</sub> [V]	j <sub>1/2</sub> [mA cm <sup>-2</sup> ]	E <sub>onset</sub> [V]	j <sub>lim(0.4V)</sub> [mA cm <sup>-2</sup> ]	ESCA [m <sup>2</sup> g <sub>Pt</sub> <sup>-1</sup> ]
1	PFCN@NT	0.828	-1.65	0.918	-4.22	64
2	PFCN@NT <sup>300</sup>	0.868	-2.22	0.953	-4.64	138
3	PFCN@NT <sup>600</sup>	0.723	-2.17	1.008	-3.93	27
4	MWCNT	0.633	-0.93	0.723	-2.11	–
5	Pt <sub>3</sub> Co@NT	0.868	-2.12	0.983	-4.28	62

root of the rotation rates. This effect originates in a shortening of the diffusion pathways with increasing rotation rates. In contrast, the ORR curves of the samples PFCN@NT and PtFeCoN@NT<sup>600</sup> (see Figure S7), exhibit shrinking distances at higher rotation rates. This points to the presence of a kinetic inhibition of the electron transfer process for these catalysts. A K–L plot (Figure 6d) obtained from the RRDE results of PFCN@NT<sup>300</sup> under various potentials shows that the slopes in the potential range from 0.3 to 0.7 V stayed almost constant, which indicates that the electron transfer number per oxygen molecule is nearly the same at the different potentials. The mean value of  $n$  calculated by Equations 1 and 2 for PFCN@NT<sup>300</sup> is 3.94, i.e., this catalyst favors the four-electron reduction process. The number of electrons transferred by O<sub>2</sub> and H<sub>2</sub>O<sub>2</sub> formed as side-product were also derived from RRDE data at 1600 rpm (data analyzed according to equations (4), and (5) in the experimental section, see also Figure S9 in the ESI). The maximum amounts of H<sub>2</sub>O<sub>2</sub> for PFCN@NT, PFCN@NT<sup>300</sup> and Pt<sub>3</sub>Co@NT were 0.13%, 0.09% and 0.18%, which confirms the number of electrons transferred by O<sub>2</sub>-molecule obtained by KL-plots. All three catalysts showed transfer 4.00 electrons and confirm the previous results.

The ECSA increased after sintering at 300 °C from 64 m<sup>2</sup>g<sub>Pt</sub><sup>-1</sup> (PFCN@NT) to 138 m<sup>2</sup>g<sub>Pt</sub><sup>-1</sup> while for sample PFCN@NT<sup>600</sup>, which had been sintered at 600 °C under Ar/H<sub>2</sub> atmosphere, the ECSA decreases due to the bigger crystallite sizes to 27 m<sup>2</sup>g<sub>Pt</sub><sup>-1</sup> (Table 1, entry 3, see also Figure S8).

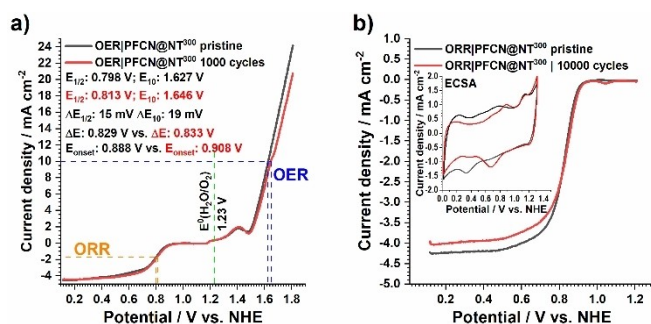


**Figure 7.** ADT for a) 1000 cycles for OER (see also Table 2) and b) 10000 Cycles for ORR in 0.1 M KOH (see also Table 3).

**Table 2.** Comparison of OER and ORR activities in 0.1 M KOH for PtFeCoNi<sup>300</sup>, Pt/C and MWCNT.

Entry	Catalyst	E <sub>1/2</sub> (ORR) [V]	E <sub>10</sub> (OER) [V]	ΔE [V]	Ref.
1	PFCN@NT <sup>300</sup>	0.798	1.627	0.829	This work
2	PFCN@NT <sup>300</sup> After OER-ADT	0.813	1.646	0.833	This work
3	Pt/C	0.82	1.86	1.04	[36]
4	MWCNT	0.71	1.88	1.17	[36]
5	NCMT-1000(3d)	0.89	1.52	0.63	[40]
6	Co <sub>3</sub> FeN	0.79	1.65	0.86	[37]
7	NiFe <sub>2</sub> O <sub>4</sub>	0.68	1.64	0.96	[38]

Because of the superior performance of PFCN@NT<sup>300</sup>, more detailed studies on the OER/ORR activities of this catalyst were carried out, namely advanced durability test (ADT) for the OER and ORR activity of the PFCN@NT<sup>300</sup> catalyst in O<sub>2</sub>-saturated 0.1 M KOH with a rotation speed of 1600 rpm were performed. Figure 7a shows the results before and after 1000 cycles OER-ADT. The ORR half-wave potential E<sub>1/2</sub> is 798 mV (after ADT 813 mV) and the onset potential is 888 mV (after ADT 908 mV). The OER potential E<sub>10</sub> at a current density of 10 mAcm<sup>-2</sup> is 1.627 V (after ADT 1.646 V), resulting in a ΔE(E<sub>10</sub>-E<sub>1/2</sub>) of 829 mV (after ADT 833 mV) which is clearly better than the performance of pure Pt/C (ΔE = 1040 mV).<sup>[36]</sup>

Table 2 summarizes the parameters derived from Figure 7a. The results indicate a significant effect of the substitution of Pt by the TMs. The ORR performance is slightly lower in onset potential and half-wave potential compared to pure Pt/C (Table 2, entry 3),<sup>[36]</sup> and MWCNTs (entry 4)<sup>[36]</sup> reported literature. This is achieved with a reduction of the Pt loading by early 75 atomic-%. A wider literature review<sup>[16,20]</sup> shows the catalyst performance to be comparable to other Co/Fe-based catalysts like Co<sub>3</sub>FeN-nanosheets<sup>[37]</sup> (entry 6), or mixed spinel-oxides<sup>[38]</sup> (entries 7 and 8). However, iron-loaded nitrogen-doped carbon-composites<sup>[39]</sup> or pure nitrogen-doped carbon catalysts<sup>[40]</sup> can reach lower potentials (entry 8) and or lower ΔE (entry 5).

Figure 7b shows the results of the ORR-ADT. Table 3 summarizes the results depicted in Figure 7b. The half-wave potential E<sub>1/2</sub> is slightly shifted to higher potentials from 838 mV to 853 mV and the respective current density j<sub>1/2</sub> shrinks by 9.4% from -1.49 to -1.35 mAcm<sup>-2</sup>. The diffusion limited current density at a potential of 300 mV decrease from -4.203 mAcm<sup>-2</sup> to -3.971 mAcm<sup>-2</sup> after 10000 cycles, which corresponds to a drop of 5.5%. The ECSA is reduced by 15.8% after 10000 cycles ORR-ADT. This indicates an activity loss either by particle detachment or agglomeration and Ostwald ripening.<sup>[41-43]</sup> Nevertheless, the remaining electrochemical ORR activity after 10000 cycles is still good and the catalyst seems to be very stable in 0.1 M KOH.

## Conclusion

In this work, an effective catalyst for ORR and OER was synthesized via a straight-forward wet chemistry route. The unique structure of a Pt-core and a TM-oxide shell shows a good durability and a stable performance in ORR and OER. The results of the PFCN@NT<sup>300</sup> catalyst indicate a significant effect of the substitution of Pt by the TM and the formation of nanoparticles on the catalytic performance especially in the

**Table 3.** Results of the ADT for ORR with PFCN@NT<sup>300</sup> in 0.1 M KOH over 10000 cycles.

PFCN@NT300	E <sub>1/2</sub> [V]	j <sub>1/2</sub> [mAcm <sup>-2</sup> ]	j <sub>lim (0.3V)</sub> [mAcm <sup>-2</sup> ]	E <sub>onset</sub> [V]	ECSA [m <sup>2</sup> gPt]
pristine	0.838	-1.49	-4.203	0.913	98.78
After 10000 cycles	0.853	-1.35	-3.971	0.918	85.26



OER. The ORR performance is slightly lower in onset potential and half-wave potential compared to pure Pt/C. However, the amount of Pt required is reduced by nearly 75 atomic-%. As a bi-functional catalyst, it displays a smaller over-potential of 0.83 V, smaller than the commercial Pt/C- or RuO<sub>2</sub>-catalysts, and in a range proven to be accessible with Co/Fe-catalysts.<sup>[37–39]</sup> Furthermore, PFCN@NT<sup>300</sup> demonstrated a remarkable stability of ORR and OER activities in aqueous electrolyte, highlighting its importance as a bi-functional catalyst in metal air battery and electrolyzers.

## Experimental Section

**Materials:** MWCNTs (Sigma Aldrich 755133-5g) were functionalized via acidic heat treatment (MWCNT → f-MWCNT).<sup>[44]</sup> All other chemicals were obtained in analytical grad quality from commercial suppliers and were used without further purification.

**Catalyst Synthesis: PFCN@NT:** Acid-functionalized MWCNT (f-MWCNT) 100 mg) were dispersed in 200 mL ethylene glycol and water (1:1) mixture, by stirring for 12 h at room temperature. 3.8 ml each of 0.05 M solutions of H<sub>2</sub>PtCl<sub>6</sub>, Fe(NO<sub>3</sub>)<sub>2</sub>, Ni(NO<sub>3</sub>)<sub>2</sub> and Co(NO<sub>3</sub>)<sub>2</sub> were then added and the mixture was stirred for another 24 h. The pH of the resulting suspension was adjusted to 11 via addition of 2.5 M aqueous NaOH and the mixture was heated to 50 °C. 50 mL of a 0.1 M NaBH<sub>4</sub>-solution was added dropwise over 1 hour. After complete addition, the solution was stirred for another 12 h and the resulting black precipitate was collected by filtration and washed with demineralized water. The isolated black powder -designated as PFCN@NT - was dried for 24 h at 100 °C in a vacuum oven. **PFCN@NT<sup>300</sup>/ PFCN@NT<sup>600</sup>:** Portions of PFCN@NT were sintered at 300 °C in an argon atmosphere for 2 h or at 600 °C in a hydrogen/argon (5 % H<sub>2</sub>) atmosphere for 3 h, respectively. These catalyst batches are designated as PFCN@NT<sup>300</sup> and PFCN@NT<sup>600</sup> in the following. **Pt<sub>3</sub>Co@NT:** As a reference, a Pt<sub>3</sub>Co@NT catalyst was synthesized by the same method as PFCN@NT.

**Structural Characterization:** X-ray diffraction (STOE STADI P, Cu-source, STOE & Cie GmbH) was used for the phase identification. The morphology and microstructure of all samples were observed by scanning electron microscopy (SEM, Zeiss Gemini) and transmission electron microscopy (TEM, Thermo Fischer Scientific Themis 300), both equipped for energy-dispersive x-ray (EDX) analysis. In order to perform the TEM measurements, the samples were prepared using a direct dispersion of the dry powders on a TEM lacey carbon membrane. No solvent was used for dispersion in order to reduce carbon contamination buildup during STEM scanning. The measurements were performed using a Themis 300 electron microscope working at 300 kV and equipped with a DCOR probe corrector and a Super-X EDX detector. The K-lines of C, O, Fe, Co, Ni and the L-lines of Pt were used for quantification in STEM-EDX. High-angle annular dark-field images (HAADF) were recorded within a collection angle range of 79 to 200 mrad, while for bright field images (BF) a collection angle of 16 mrad was employed.

The elemental composition and the chemical state of the samples was analyzed by X-ray photoelectron spectroscopy (XPS) measurements (PHI 5800 MultiTechnique ESCA System, Physical Electronics) using monochromatized Al K $\alpha$  radiation (250 W, 15 kV), a detection angle of 45°, and pass energies of 93.9 and 29.35 eV at the analyzer for survey and detail measurements, respectively. It should be mentioned that XPS is a surface sensitive method with a sampling

depth in the range of several nanometers. Charging effects were negligible for the samples. General binding energy calibration of the XPS instrument was done before the measurement by adjusting the instrument work function using a metallic Ag specimen (Ag 3d<sub>5/2</sub> peak to 368.3 eV)<sup>[23,24]</sup> The peak fit of the results was done with CasaXPS, using Shirley-type backgrounds and Gaussian-Lorentzian peak shapes (except of the C 1s peak of graphitic C and the Pt 4f peak doublet of metallic Pt, where an asymmetric shape is expected). For the peak doublets, both the intensity ratio (4:3 for Pt 4f and 2:1 for Fe 2p, Co 2p and Ni 2p) and the spin-orbit splitting were set to the expected values.<sup>[23,24]</sup> For the calculations of corrected peak intensities, the relative sensitivity factors of the instrument manufacturer (Physical Electronics) were used. Throughout the composite catalyst synthesis, Raman spectra were collected from the samples at different stages in the spectral range of 100–4000 cm<sup>-1</sup> by using an inVia™ confocal Raman microscope (RENISHAW) with a 633 nm excitation laser, 1 mW average laser power and 10 s exposer time. In the confocal system, a grating was used as dispersion element with a groove density of 1800 mm<sup>-1</sup>, while a 50X (0.75 NA) objective was used in back scattering geometry to collect all the Raman spectra.

**Electrochemical Characterization:** The electrochemical measurements were performed at room temperature in a three-electrode setup using a bipotentiostat WaveDriver20 together with a rotating ring-disc electrode-setup (RRDE) from Pine Research Instruments. An Ag/AgCl-reference electrode filled with 3.5 M KCl solution and Pt-wire counter electrode were used in the experiments. The glassy carbon working electrode with a surface area of 0.19635 cm<sup>2</sup> was coated with 5  $\mu$ L of well-dispersed catalyst ink. The ink was prepared by adding 20 mg active material to a mixture of 50  $\mu$ L Nafion suspension (20 wt. % in lower aliphatic alcohols and water, contains 34% water) and 1950  $\mu$ L ethanol. The catalyst ink was stirred for 24 h and sonicated in an ultra-sonic bath for 10 min before use. The active material (catalyst + supporting material) loading of the working electrode was 0.25 mg cm<sup>-2</sup>. Background cyclic voltammetry curves were recorded between –0.95 V and 0.35 V versus Ag/AgCl with a scan speed of 10 mV s<sup>-1</sup> in N<sub>2</sub>-saturated 0.1 M KOH solution. Measurements with a scan speed of 50 mV s<sup>-1</sup> were used to determine the electrochemically active surface area (ECSA) via normalizing the charge integral between –0.95 V and 0.05 mV versus Ag/AgCl without double layer corrections.<sup>[45]</sup>

The ORR experiments were investigated in O<sub>2</sub>-saturated 0.1 M KOH solution at rotation speeds between 100 and 3025 rpm and with a scan speed of 10 mV s<sup>-1</sup>. Two types of accelerated durability tests (ADTs) were performed. While 10000 cycles start/stop were carried out between –0.3 V and 0.1 V versus Ag/AgCl with a scan speed of 100 mV s<sup>-1</sup> for ORR, 1000 cycles start/stop between 0.15 V and 0.85 V versus Ag/AgCl with a scan speed of 100 mV s<sup>-1</sup> were done for OER.

ORR/OER cyclic voltammetry curves were accomplished between –0.95 V and 0.85 V versus Ag/AgCl with a scan speed of 10 mV s<sup>-1</sup>.

The kinetic current density  $j_k$  can be determined via Koutecky-Levich (K–L) equation (1) where  $j$  is the measured current density and  $j_L$  is the diffusion limited current density.

$$j^{-1} = j_L^{-1} + j_k^{-1} \quad (1)$$

$$j_L = 0.62 \cdot n \cdot F \cdot D_o^{2/3} \cdot C_o \cdot \nu^{-1/6} \cdot \omega^{1/2} \quad (2)$$

In addition,  $j_L$  can be described by the Levich equation (2) where  $n$  is the number of involved electrons transferred during ORR;  $F$  is the faraday constant ( $96485 \text{ C mol}^{-1}$ );  $\omega$  is the rotation speed in  $\text{rad s}^{-1}$ ;  $D_{\text{O}}$  is the diffusion coefficient of  $\text{O}_2$  in  $0.1 \text{ M KOH}$  ( $1.9 \cdot 10^{-5} \text{ cm}^2 \text{ s}^{-1}$ );  $C_{\text{O}}$  is the bulk concentration of oxygen ( $1.2 \cdot 10^{-6} \text{ mol cm}^{-3}$ ) and  $\nu$  is the kinematic viscosity of the electrolyte ( $0.01 \text{ cm}^2 \text{ s}^{-1}$ ).

All electrochemically measurements were performed at room temperature and the potential was converted to RHE via equation

$$E_{\text{RHE}} = E_{\text{Ag/AgCl}} + E_{\text{Ag/AgCl}}^0 + 0.059 \cdot \text{pH} \quad (3)$$

where  $E_{\text{Ag/AgCl}}$  is the measured potential vs Ag/AgCl,  $E_{\text{Ag/AgCl}}^0 = 0.1976$  at  $25^\circ\text{C}$  and pH of the used electrolyte ( $0.1 \text{ M KOH}$ ,  $\text{pH} = 13$ ).

The amount of  $\text{H}_2\text{O}_2$  ( $\chi\text{-H}_2\text{O}_2$ ) was calculated via equation (4).

$$\chi\text{-H}_2\text{O}_2 = (200 \cdot I_{\text{ring}}/N)/(I_{\text{disc}} + I_{\text{ring}}/N) \quad (4)$$

with transmission rate  $N = 25.6$

The number of electrons transferred ( $n_{(e^-)}$ ) was derived via equation (5).

$$n_{(e^-)} = 4 \cdot I_{\text{disc}}/(I_{\text{disc}} + I_{\text{disc}}/N) \quad (5)$$

## Supporting Information Summary

The ESI includes details on XPS peak fitting, graphs, images and spectra from XPS, XRF, SEM/EDX and HAADF measurements, as well as supplementary graphs summarizing electrocatalytic performance. A file containing the raw electrochemical data prior to processing is also included.

## Acknowledgements

The authors acknowledge the financial support of Steinbeis Transferzentrum Angewandte Elektronik at the Hochschule Heilbronn. This work contributes to the research performed at CELEST (Center for Electrochemical Energy Storage Ulm-Karlsruhe). Authors gratefully acknowledge financial support by Deutsche Forschungsgemeinschaft (DFG, German Research Foundation) under Germany's Excellence Strategy, EXC 2154, project number 390874152. A thanks goes to Andreas Gruber for the opportunity to carry out XRF measurements. Open Access funding enabled and organized by Projekt DEAL.

## Conflict of Interests

The authors declare no conflict of interest.

## Data Availability Statement

The data that support the findings of this study are available in the supplementary material of this article.

**Keywords:** bifunctional electrocatalyst · core-shell nanoparticles · electrocatalysis · OER · ORR

- [1] Y. Wang, D. F. Ruiz Diaz, K. S. Chen, Z. Wang, X. C. Adroher, *Mater. Today* **2020**, *32*, 178.
- [2] S. Zaman, L. Huang, A. I. Douka, H. Yang, B. You, B. Y. Xia, *Angew. Chem.* **2021**, *133*, 17976.
- [3] M. A. Abdelkareem, K. Elsaid, T. Wilberforce, M. Kamil, E. T. Sayed, A. Olabi, *Sci. Total Environ.* **2021**, *752*, 141803.
- [4] T. Braun, S. Dinda, F. Pammer, M. Fichtner, *ChemElectroChem* **2022**, *9*, e202101191.
- [5] F. Cheng, J. Chen, *Chem. Soc. Rev.* **2012**, *41*, 2172.
- [6] Y. Sun, X. Liu, Y. Jiang, J. Li, J. Ding, W. Hu, C. Zhong, *J. Mater. Chem. A* **2019**, *7*, 18183.
- [7] X. Wu, C. Tang, Y. Cheng, X. Min, S. P. Jiang, S. Wang, *Chem. Eur. J.* **2020**, *26*, 3906.
- [8] J. Rossmel, Z.-W. Qu, H. Zhu, G.-J. Kroes, J. K. Nørskov, *J. Electroanal. Chem.* **2007**, *607*, 83.
- [9] D. Liu, Y. Tong, X. Yan, J. Liang, S. X. Dou, *Batteries & Supercaps* **2019**, *2*, 743.
- [10] Q. Liang, G. Brocks, A. Bieberle-Hütter, *J. Phys. Energy* **2021**, *3*, 026001.
- [11] X. Ren, Q. Lv, L. Liu, B. Liu, Y. Wang, A. Liu, G. Wu, *Sustain. Energy Fuels* **2020**, *4*, 15.
- [12] A. Mahata, A. S. Nair, B. Pathak, *Catal. Sci. Technol.* **2019**, *9*, 4835.
- [13] S. Sui, X. Wang, X. Zhou, Y. Su, S. Riffat, C. Liu, *J. Mater. Chem. A* **2017**, *5*, 1808.
- [14] C. Zhang, X. Shen, Y. Pan, Z. Peng, *Front. Energy* **2017**, *11*, 268.
- [15] N.-T. Suen, S.-F. Hung, Q. Quan, N. Zhang, Y.-J. Xu, H. M. Chen, *Chem. Soc. Rev.* **2017**, *46*, 337.
- [16] T. Noor, L. Yaqoob, N. Iqbal, *ChemElectroChem* **2021**, *8*, 447.
- [17] G. C. da Silva, M. R. Fernandes, E. A. Ticianelli, *ACS Catal.* **2018**, *8*, 2081.
- [18] J. Du, J. Quinson, D. Zhang, F. Bizzotto, A. Zana, M. Arenz, *ACS Catal.* **2021**, *11*, 820.
- [19] S. J. Hwang, S. J. Yoo, S. Jang, T.-H. Lim, S. A. Hong, S.-K. Kim, *J. Phys. Chem. C* **2011**, *115*, 2483.
- [20] C. X. Zhao, J. N. Liu, J. Wang, D. Ren, B. Q. Li, Q. Zhang, *Chem. Soc. Rev.* **2021**, *50*, 7745.
- [21] X. Chen, H. Wang, Y. Wang, Q. Bai, Y. Gao, Z. Zhang, *Catalysts* **2015**, *5*, 1003.
- [22] P. Mukherjee, B. Kakade, A. Swami, *Energy Fuels* **2022**, *36*, 2306.
- [23] D. Briggs, C. D. Wanger, W. M. Riggs, L. E. Davis, J. F. Moulder, G. E. Muilenberg, *Handbook of X-ray Photoelectron Spectroscopy* (Ed.: Perkin-Elmer Corp., Physical Electronics Division, Eden Prairie, Minnesota, U.), **1981**.
- [24] J. F. Moulder, W. F. Stickle, P. E. Sobol, K. D. Bomben, *Handbook of X-ray photoelectron spectroscopy. Update.*, Perkin-Elmer Corporation, Eden Prairie, Minn., **1992**.
- [25] L. Wang, D. Mercier, S. Zanna, A. Seyeux, M. Laurent-Brocq, L. Perrière, I. Guillot, P. Marcus, *Corros. Sci.* **2020**, *167*, 108507.
- [26] B. J. Tan, K. J. Klabunde, P. M. A. Sherwood, *J. Am. Chem. Soc.* **1991**, *113*, 855.
- [27] M. C. Biesinger, B. P. Payne, A. P. Grosvenor, L. W. M. Lau, A. R. Gerson, R. S. C. Smart, *Appl. Surf. Sci.* **2011**, *257*, 2717.
- [28] S. Ekerth, J. Ekspong, D. K. Perivoliotis, S. Sharma, R. Boyd, N. Brenning, E. Gracia-Espino, L. Edman, U. Helmersson, T. Wågberg, *ACS Appl. Nano Mater.* **2021**, *4*, 12957.
- [29] R. M. Balabai, H. N. Chernikova, *Appl. Phys. A Mater. Sci. Process.* **2014**, *116*, 649.
- [30] Z.-Y. Wang, B. Zhang, S. Liu, G.-R. Li, T. Yan, X.-P. Gao, *Adv. Funct. Mater.* **2022**, *32*, 2200893.
- [31] C. Moreira Da Silva, A. Girard, M. Dufond, F. Fossard, A. Andrieux-Ledier, V. Huc, A. Loiseau, *Nanoscale Adv.* **2020**, *2*, 3882.
- [32] L. G. Cançado, A. Jorio, E. H. M. Ferreira, F. Stavale, C. A. Achete, R. B. Capaz, M. V. O. Moutinho, A. Lombardo, T. S. Kulmala, A. C. Ferrari, *Nano Lett.* **2011**, *11*, 3190.
- [33] A. J. Bard, L. R. Faulkner, *Electrochemical methods: fundamentals and applications*, Wiley New York, **2001**.
- [34] C. Breitkopf, K. Swider-Lyons, *Springer Handbook of Electrochemical Energy* (Eds.: Breitkopf, C.; Swider-Lyons, K.), Springer Berlin Heidelberg, Berlin, Heidelberg, **2017**.
- [35] C. H. Hamann, W. Vielstich, *Elektrochemie*, 4th ed., Wiley-VCH, Weinheim, **2005**.
- [36] Y. Liu, H. Jiang, Y. Zhu, X. Yang, C. Li, *J. Mater. Chem. A* **2016**, *4*, 1694.



- [37] H.-P. Guo, X.-W. Gao, N.-F. Yu, Z. Zheng, W.-B. Luo, C. Wu, H.-K. Liu, J.-Z. Wang, *J. Mater. Chem. A* **2019**, *7*, 26549.
- [38] C. Si, Y. Zhang, C. Zhang, H. Gao, W. Ma, L. Lv, Z. Zhang, *Electrochim. Acta* **2017**, *245*, 829.
- [39] K. Mamtani, D. Jain, A. C. Co, U. S. Ozkan, *Energy Fuels* **2017**, *31*, 6541.
- [40] J.-C. Li, P.-X. Hou, S.-Y. Zhao, C. Liu, D.-M. Tang, M. Cheng, F. Zhang, H.-M. Cheng, *Energy Environ. Sci.* **2016**, *9*, 3079.
- [41] S. Cherevko, N. Kulyk, K. J. J. Mayrhofer, *Nano Energy* **2016**, *29*, 275.
- [42] J. C. Meier, C. Galeano, I. Katsounaros, J. Witte, H. J. Bongard, A. A. Topalov, C. Baldizzone, S. Mezzavilla, F. Schüth, K. J. J. Mayrhofer, *Beilstein J. Nanotechnol.* **2014**, *5*, 44.
- [43] K. Yu, D. J. Groom, X. Wang, Z. Yang, M. Gummalla, S. C. Ball, D. J. Myers, P. J. Ferreira, *Chem. Mater.* **2014**, *26*, 5540.
- [44] N. T. Hung, N. M. Tuong, E. G. Rakov, *Inorg. Mater.* **2010**, *46*, 1077.
- [45] F. J. Vidal-Iglesias, R. M. Arán-Ais, J. Solla-Gullón, E. Herrero, J. M. Feliu, *ACS Catal.* **2012**, *2*, 901.

Submitted: February 2, 2023

Accepted: June 1, 2023